ARTICLE IN PRESS

Nature Communications

https://doi.org/10.1038/s41467-026-69504-y

Article in Press

# Histidine-rich coiled-coils promote zinc-dependent self-assembly and curing of porous mussel glues

Received: 6 August 2025

Accepted: 2 February 2026

Cite this article as: Rivard, M.D., Poulhazan, A., Renner-Rao, M.J. *et al.* Histidine-rich coiled-coils promote zinc-dependent self-assembly and curing of porous mussel glues. *Nat Commun* (2026). https://doi.org/10.1038/s41467-026-69504-y

**Mathieu D. Rivard, Alexandre Poulhazan, Max J. Renner-Rao, Emilie Duthoo, Franziska Jehle, Patrick Flammang, Daniel J. Jackson & Matthew J. Harrington**

We are providing an unedited version of this manuscript to give early access to its findings. Before final publication, the manuscript will undergo further editing. Please note there may be errors present which affect the content, and all legal disclaimers apply.

If this paper is publishing under a Transparent Peer Review model then Peer Review reports will publish with the final article.

ARTICLE IN PRESS

© The Author(s) 2026. **Open Access** This article is licensed under a Creative Commons Attribution-NonCommercial-NoDerivatives 4.0 International License, which permits any non-commercial use, sharing, distribution and reproduction in any medium or format, as long as you give appropriate credit to the original author(s) and the source, provide a link to the Creative Commons licence, and indicate if you modified the licensed material. You do not have permission under this licence to share adapted material derived from this article or parts of it. The images or other third party material in this article are included in the article's Creative Commons licence, unless indicated otherwise in a credit line to the material. If material is not included in the article's Creative Commons licence and your intended use is not permitted by statutory regulation or exceeds the permitted use, you will need to obtain permission directly from the copyright holder. To view a copy of this licence, visit http://creativecommons.org/licenses/by-nc-nd/4.0/.

# Histidine-rich coiled-coils promote zinc-dependent self-assembly and curing of porous mussel glues

Mathieu D. Rivard[1], Alexandre Poulhazan[1], Max J. Renner-Rao[1], Emilie Duthoo[2], Franziska Jehle[1,3], Patrick Flammang[2], Daniel J. Jackson[4], Matthew J. Harrington[1]*

[1]Dept. of Chemistry, McGill University; 801 Sherbrooke Street West, Montreal, Quebec H3A 0B8, Canada.

[2]Biology of Marine Organisms and Biomimetics Unit, Research Institute for Biosciences, University of Mons, Place du Parc 23, B-7000 Mons, Belgium

[3]Department of Biomaterials, Max Planck Institute of Colloids and Interfaces, Am Mühlenberg 1, 14476 Golm, Germany

[4]Department of Geobiology, Georg-August University of Göttingen, Goldschmidtstr. 3, 37077, Göttingen, Germany

***Corresponding Author:** matt.harrington@mcgill.ca

## Abstract

Challenging to engineer in synthetic glues, wet adhesion is critical for many technical and biomedical applications. Mussels, however, have evolved underwater glues that adhere effectively onto slippery seashore surfaces. Past research on mussel adhesion highlights the importance of the post-translationally modified amino acid 3,4-dihydroxyphenylalanine (DOPA), found in abundance in mussel glue proteins. Yet, DOPA alone is insufficient to match native adhesion in synthetic mimics. Here, we provide evidence that a previously uncharacterized histidine-rich protein (mefp-12) plays a crucial role in the formation, curing, and performance of mussel glue. Biochemical analysis localizes mefp-12 within vesicles of the mussel glue secretory glands, while AI-assisted modeling of its sequence predicts Zn-stabilized coiled coil conformation and several domains resembling zinc-finger motifs. *In vitro* investigation of a His-rich $\alpha$-helical peptide from mefp-12 shows Zn- and pH-dependent liquid-liquid phase separation (LLPS), coalescence, and spreading over the substrate. Exposure to seawater pH induces

subsequent self-organization of the fluid condensates into solid nanoporous networks resembling the structure of the native mussel glue. Based on these findings we gain a deeper mechanistic understanding of mussel glue formation and function that challenges the dominant DOPA-centric paradigm, providing inspiration for design of bio-inspired wet adhesives.

## Introduction

Nature offers inspiration for the design of sustainable, high-performance materials of the future[1,2]. Mussels are prominent archetypes for bio-inspired wet adhesion, exhibiting a conspicuous ability to stick to slippery seashore surfaces[3]. Marine mussels (*Mytilus spp.*) anchor in intertidal habitats using acellular, protein-based fibers known as byssal threads (Fig. 1A)[2]. Byssal threads possess a highly effective underwater glue with an interconnected (open-cell) micro- and nano-porous structure called the plaque, which attaches firmly to different surfaces in seawater conditions, securing mussels against crashing waves (Fig. 1A)[3]. Many decades of biochemical investigations have identified five plaque-specific proteins (mfp-2 to mfp-6; mfp = mussel foot protein) hypothesized to have specific functions and to be localized to particular regions of the plaque (Fig. 1A, Supplementary Table 1)[3-7]. In terms of nomenclature, species-specific mussel foot proteins are denoted according to the species they come from – e.g., mfp-3 from *Mytilus edulis* is called mefp-3 while that from *Mytilus californianus* is called mcfp-3.

The versatility and prowess of mussel adhesion was previously ascribed to the presence of an atypical posttranslational modification of tyrosine prominent in these glue proteins – 3,4-dihydroxyphenylalanine (DOPA)[3,8]. Functional studies revealed that DOPA interacts directly with substrate surface chemistry through diverse non-covalent and covalent interactions, while in the bulk plaque, DOPA forms cohesive metal coordination interactions with iron and vanadium ions[3,8,9]. The identification of the role of DOPA in mussel adhesion helped establish the field of mussel-inspired materials[8], which has grown substantially over the last two decades[1,10-12]. Although impressive, these synthetic systems still do not match the properties of the native mussel adhesive[1]. To advance the field of bio-inspired adhesion, it is essential to more precisely understand the biochemical design and physicochemical control of native mussel glue formation and function, which requires examining the process by which the native plaque is produced.

In a process unlike anything found in synthetic adhesives, mussels fabricate the plaque using a secretory organ, known as the foot, in which plaque protein precursors are mass-produced and packaged in micron-scale secretory vesicles as fluid condensates, which are stockpiled with specialized secretory glands (Fig. 1B-C)[9,13,14]. Recent findings suggest that during byssus formation, plaque condensates are flowed through microfluidic-like channels and triggered to solidify by a pH increase going from the acidic storage phase (pH 3-4) to alkaline seawater (pH 8.2)[15], resulting in the spontaneous formation of the open-cell porous structure of the native plaque[9,14]. Recent studies indicate that the pores of the native plaque (pore size ranging from 0.2 µm – 2 µm[16,17]) are filled with fluid condensate glue proteins, proposed to extend the functional lifetime of the glue (Fig. 1)[14,18]. In particular, the DOPA-rich adhesive proteins (mfp-3 and mfp-5) and Cys-rich reducing protein (mfp-6) are thought to be localized at the plaque-surface interface and also within the pores where they play key roles in establishing a strong interfacial adhesion (Fig. 1A) [18]. The solid porous scaffold, on the other hand, remains understudied, despite its importance in dissipating energy from crashing waves[14,19]. Indeed, besides the presence of the protein mfp-2[4], surprisingly little is understood about scaffold composition, the biochemical structure-function relationships that define its behavior, or the spontaneous self-assembly of its porous structure.

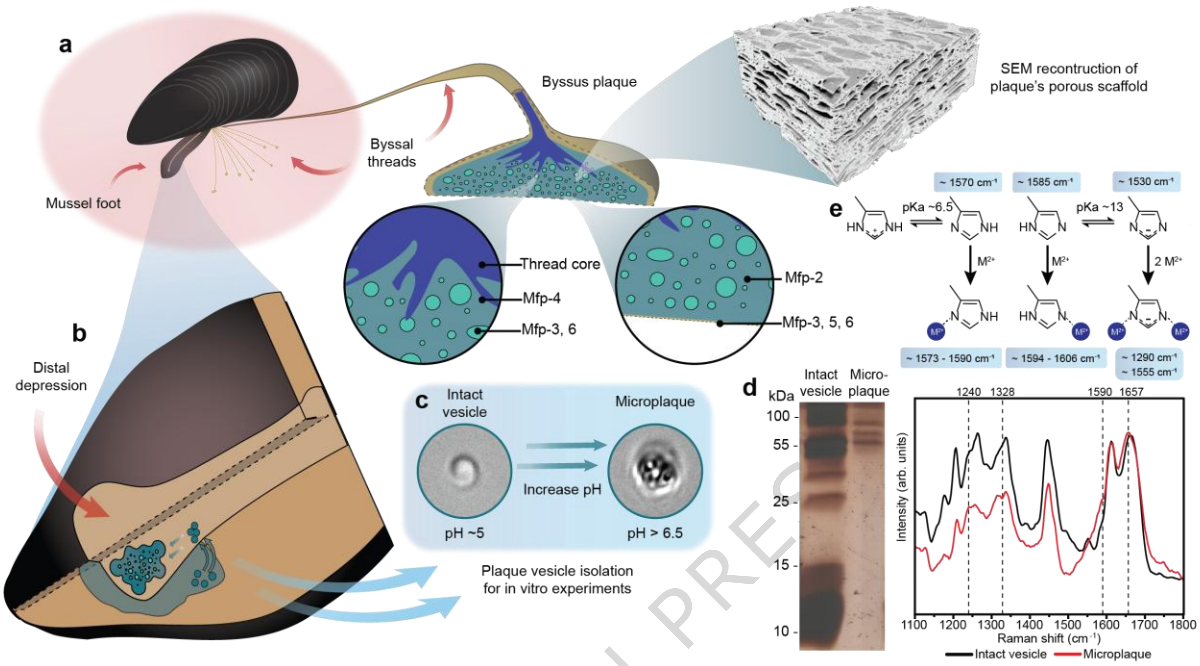

**Figure 1. Self-assembly of porous mussel glue. a** Mussels attach to surfaces using byssal threads, which terminate at the plaque – a porous underwater glue made of different proteins precisely localized in the plaque. The plaque comprises a solid scaffold and fluid condensate glue proteins trapped within the pores. **b** Byssal threads are produced by a secretory organ known as the foot. Plaque proteins are stored in vesicles within the foot plaque secretory gland as fluid condensate droplets, which are secreted into the distal depression in the foot where they begin to solidify. **c** When they burst, purified plaque vesicles undergo salt- and pH-dependent liquid-liquid phase separation (LLPS) and subsequent solidification, forming a porous microplaque. **d** Microplaque-specific proteins are enriched in histidine, and Raman spectroscopy suggests the presence of histidine metal coordination cross-linking and partial alpha helical secondary structure in microplaques, based on peak positions denoted by dashed lines. **e** Schematic of pH-dependent histidine deprotonation and metal binding with associated characteristic Raman peaks noted.

Recently, we developed a method to extract and purify intact plaque secretory vesicles from the mussel foot glands[14], which contain all of the protein components used to make the plaque. This enabled direct analysis of the proteins as well as *in vitro* assembly studies under defined physicochemical conditions. Several key observations emerged from these initial studies[14,20]: 1) Plaque vesicles from the blue mussel *Mytilus edulis* contain at least ten different proteins[14,20] (contrasting the five proteins currently confirmed to be present in the plaque). This indicates at least five uncharacterized plaque proteins, which could be playing important roles in plaque formation and function. 2) Several of the uncharacterized proteins in the vesicles stained positively for elevated content of the amino acid histidine[14]. Notably, previous transcriptomic analysis on a related mussel species identified several putative byssus glue proteins enriched in histidine[21], while very recent studies identified similar histidine-rich proteins stored within the plaque secretory vesicles of *M. edulis*[20]. 3) It was observed that when the plaque vesicle membrane was osmotically ruptured, the condensate within self-assembled into a nanoporous solid structure reminiscent of the native plaque. Specifically, the condensate spontaneously underwent pH-dependent LLPS in which certain proteins rapidly cured into a solid "microplaque" with native-like porous structure, while other proteins remained as fluid condensates in the pores that eventually washed away into the buffer (Fig. 1C)[14]. Importantly, the critical pH for inducing solidification is close to the $pK_a$ of histidine (pH ~6.5), suggesting a possible role of the unknown His-rich proteins in plaque self-assembly and curing[1,3]. 4) The dissolution of the solidified microplaque under acidic conditions revealed the enrichment of these same unidentified higher molecular weight histidine-rich proteins from the *M. edulis* plaque vesicles. In contrast, the known lower molecular weight DOPA-rich proteins (MW < 15 kDa), which based on previous studies remain as a fluid condensate phase[14,22], were washed away from solid scaffold following vesicle rupture leaving only the scaffold histidine-rich proteins in the solid microplaque (Fig. 1D).

Based on these clues, we hypothesize that these as of yet uncharacterized histidine-rich plaque proteins may play a pivotal role in the self-organization and curing during plaque formation by undergoing phase separation to form the solid open-cell porous network structure of the plaque. This porous morphology is crucial to glue performance in terms of both mechanics[19] and redox regulation[18]. Here, we aim to investigate these uncharacterized plaque scaffold proteins, characterize their properties, and understand their role in formation and function of mussel glue.

## Results

### *mefp-12 is an evolutionarily conserved histidine-rich plaque protein in Mytilid mussels*

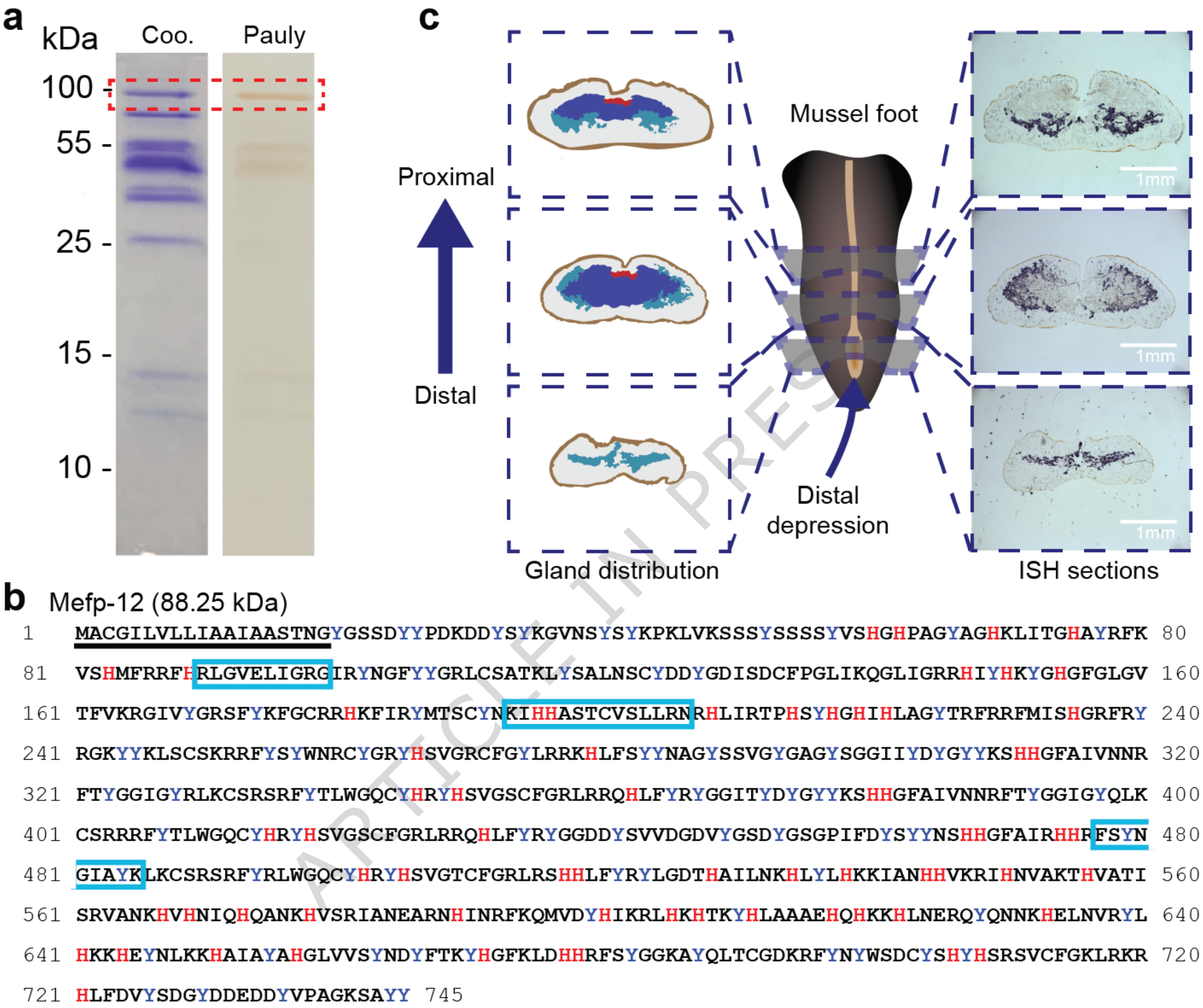

```
1   MACGILVLLIAAIAASTNGYGSSDYYPDKDDYSYKGVNSYSYKPKLVKSSSYSSSSYVSHGHPAGYAGHKLITGHAYRFK 80
81  VSHMFRRFHRLGVELIGRGIRYNGFYYGRLCSATKLYSALNSCYDDYGDISDCFPGLIKQGLIGRRHIYHKYGHGFGLGV 160
161 TFVKRGIVYGRSFYKFGCRRHKFIRYMTSCYNKIHHASTCVSLLRNRHLIRTPHSYHGHIHLAGYTRFRRFMISHGRFRY 240
241 RGKYYKLSCSKRRFYSYWNRCYGRYHSVGRCFGYLRRKHLFSYYNAGYSSVGYGAGYSGGIIYDYGYYKSHHGFAIVNNR 320
321 FTYGGIGYRLKCSRSRFYTLWGQCYHRYHSVGSCFGRLRRQHLFYRYGGITYDYGYYKSHHGFAIVNNRFTYGGIGYQLK 400
401 CSRRRFYTLWGQCYHRYHSVGSCFGRLRRQHLFYRYGGDDYSVVDGDVYGSDYGSGPIFDYSYYNSHHGFAIRHHRFSYN 480
481 GIAYKLKCSRSRFYRLWGQCYHRYHSVGTCFGRLRSHHLFYRYLGDTHAILNKHLYLHKKIANHHVKRIHNVAKTHVATI 560
561 SRVANKHVHNIQHQANKHVSRIANEARNHINRFKQMVDYHIKRLHKHTKYHLAAAEHQHKKHLNERQYQNNKHELNVRYL 640
641 HKKHEYNLKKHAIAYAHGLVVSYNDYFTKYHGFKLDHHRFSYGGKAYQLTCGDKRFYNYWSDCYSHYHSRSVCFGKLRKR 720
721 HLFDVYSDGYDDEDDYVPAGKSAYY 745
```

**Figure 2. Localization and sequence elucidation of the histidine-rich adhesive protein mefp-12 in *Mytilus edulis*. a** Plaque vesicles contain the histidine rich protein mefp-12, confirmed with Pauly staining of SDS gels (**a**: *N* = 2 gels from 2 specimens). **b** Sequence of mefp-12 (from *Mytilus edulis*) with signal sequence underlined in black, histidine residues highlighted in red, and MS/MS confirmed peptides boxed (Genbank Accession: PV698367**). c** *In-situ* hybridization (ISH) shows that mefp-12 is produced exclusively in the plaque secretory gland corresponding to the green regions of the

illustrated foot cross-sections (blue and red regions correspond to the core and cuticle glands, respectively).

To investigate the composition of the porous plaque scaffold material, we induced the formation of solid microplaques by rupturing purified plaque vesicles under basic conditions. After washing the fluid proteins away from the pores, the solid microplaques were dissolved under acidic conditions, yielding solubilized scaffold proteins. SDS-PAGE analysis identified several prominent bands (Fig. 1D) that correspond to plaque vesicle proteins that stain positively for Pauly stain (histidine-specific) (Fig. 2A and Supplementary Fig. 1)[23]. Recent investigations of whole plaque vesicle extracts identified the presence of several previously uncharacterized histidine enriched proteins[20] – however, the localization of these proteins in the plaque and their potential function remains unknown. To determine if these proteins might correspond to the proteins extracted from the solid microplaque, MS-MS proteomic analysis was performed on tryptic peptides extracted specifically from the highest molecular weight band on the SDS gel, which stained strongest for histidine (Fig. 2A). MS/MS analysis identified a single protein-coding transcript that was abundantly expressed in a *Mytilus edulis* plaque gland transcriptome[24] and previously identified as a component of the plaque vesicles through whole vesicle proteomic analysis[20].

The corresponding full-length mRNA sequence for this transcript was obtained through a 5’ and 3’ RACE (rapid amplification of cDNA ends) approach, which revealed sequence similarity to a putative plaque protein (mcfp-12) previously identified from the transcriptome of the California mussel (*Mytilus californianus*)[21], but unverified to be present in the plaque. Consistent with this earlier nomenclature, we name the homologous protein discovered in *Mytilus edulis* mefp-12 (Fig. 2B)[20]. *In situ* hybridization using a specific DIG-labelled RNA probe confirmed the presence of mRNA transcripts coding for mefp-12 localized in plaque secretory glands of mussel foot tissue sections (Fig. 2C) and not the other glands (Fig. 2C and Supplementary Fig. 2). Further BLAST searches identified uncharacterized putative sequences homologous to mefp-12 in *Mytilus galloprovincialis, Mytilus trossulus*, and *Mytilus coruscus* with high confidence (e-values between 1e-86 to 1e-66). Although separated by at least 182.8 MYA[25], there are clear sequence similarities across all 5 mytilid species (Fig. 3A, Supplementary Table 1) with especially strong conservation of the prominent histidine residues (comprising 9.1 mol%) (Fig. 3A). Further BLAST searches against closely related non-Mytilid bivalves such as *Dreissena polymorpha* and *Dreissena rostriformis* were far less significant (e-values of 1e-3 and no hit respectively) suggesting that mefp-12 is restricted to the Mytilidae. Together, these findings confirm that mefp-12 is an evolutionarily conserved histidine-rich byssus glue protein within the Mytilus genus.

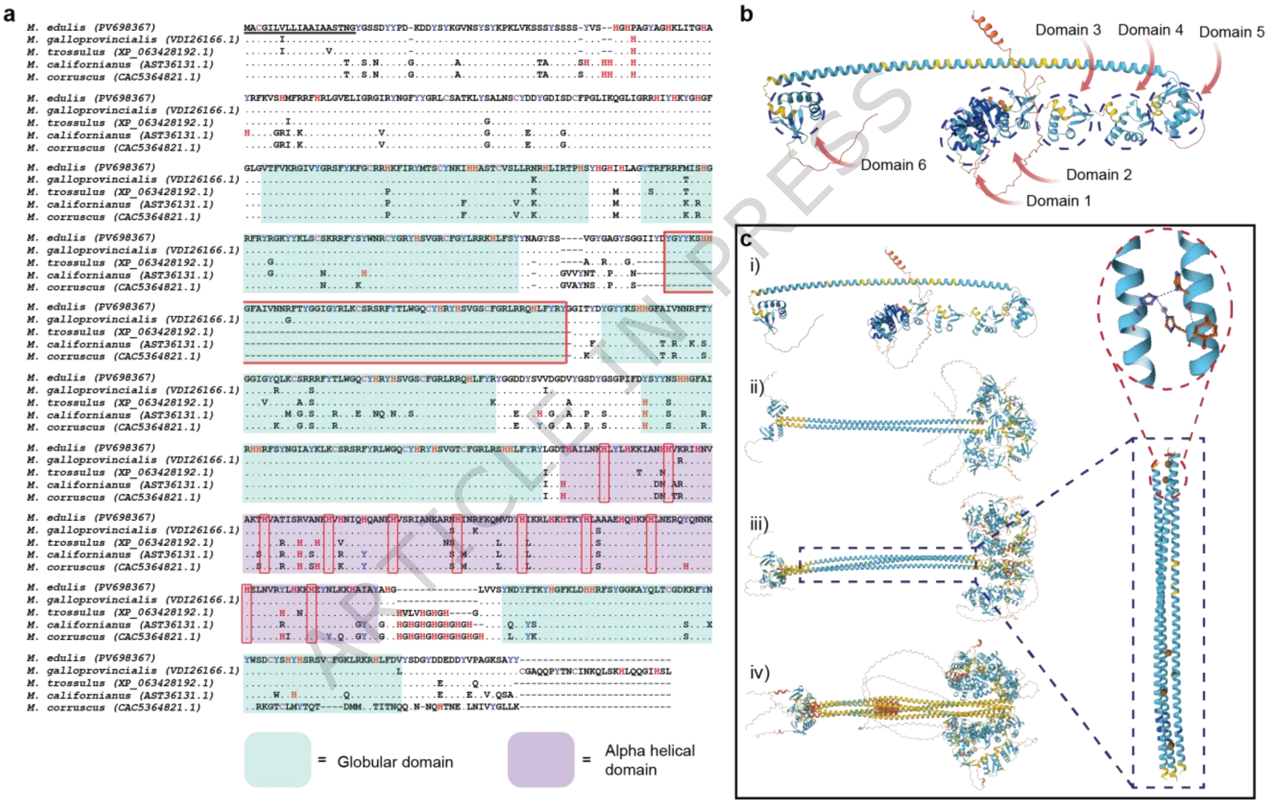

**Figure 3. Analysis of mefp-12 sequence homology and *in silico* predicted structure, oligomerization, and metal-binding. a** Comparison of mefp-12 sequences from other mytilid mussels with dots indicating conserved amino acids across species and dashes indicating gaps, highlighting the strong homology (notably in repetitive globular domains highlighted in green and the central helical domain highlighted in lavender). Conserved histidine residues within the helical domain are boxed in red. A 6th globular domain, contoured in red, is present exclusively in *M. edulis* and *M. galloprovincialis*. **b** AlphaFold3 structural prediction of Mefp-12, with repeated globular domains highlighted. **c** Monomeric

to tetrameric conformational structures predicted for mefp-12, highlighting oligomerization and Zn-binding of CC domain ($Zn^{2+}$ appears as orange spheres, confidence < 50%).

### *mefp-12 is a Zn-stabilized coiled-coil protein with prominent Zn-finger-like domains*

Building off recent investigations[20], we investigated the conformation of mefp-12 using AI-guided structural prediction algorithms. Both AlphaFold3 and Chai predicted a high degree of regular conformation for mefp-12 (Figs. 3B-C and Supplementary Figs. 3 and 4) with an extended central alpha helical domain (confidence >90%) consisting of 129 amino acids of which ~18 mol% are histidine (Supplementary Fig. 5). It was further predicted by AlphaFold and the WaggaWagga algorithm[26] that these helices will form stable coiled coils (CCs), likely homotrimeric, which possess histidine-Zn metal coordination sites within the core of the coil (Figs. 3B-C and 4A, Supplementary Figs. 6 and 7). This is unusual as CCs are typically stabilized by hydrophobic interactions between apolar residues within the CC core (Supplementary Fig. 6)[27]. While the location of zinc ions is predicted with relatively low confidence in AlphaFold (confidence <50%, Fig. 3C), the suggested binding of metal ions within the core of the CCs was intriguing as a potential zinc-dependent assembly mechanism, warranting further investigation below.

Beyond the CC domain, AlphaFold3 predicted with high confidence the presence of six domains in the terminal regions of mefp-12 possessing a common tertiary structure enriched in beta sheets and alpha helices, with conformational homology to Zn-finger motifs (Fig. 3B and Supplementary Fig. 8). There is a particularly strong conservation of histidine and cysteine residues, which are important in expected canonical $Zn^{2+}$ binding sites (Supplementary Fig. 8)[28]. Both putative zinc-binding motifs are noteworthy in the context of thread assembly as zinc is known to play a crucial pH-dependent role in the assembly of its collagenous core through His-Zn binding[29,30]. While its role within the thread core is well established, zinc has also been identified within the plaque at levels more than twice as high as that of the threads[31]. Yet, its function within the glue has yet to be elucidated.

If these computational predictions are correct, we expect to observe a dominant alpha helical structure in the plaque scaffold, as well as evidence of His-Zn metal coordination. Confocal Raman spectroscopy can assess both hypotheses. Along these lines, there are clear differences in the Raman spectra of intact plaque vesicles, which contain all plaque proteins and the microplaques (formed from ruptured vesicles at pH >6), which contain only the proteins in the solid plaque scaffold. In particular, we observe a shift of the amide I peak intensity of the microplaques to lower values (1657 $cm^{-1}$) and a shift in the relative intensity of the peaks within the amide III band with a maximum at 1328 $cm^{-1}$. Both of these changes are consistent with a shift toward more alpha helical secondary structure based on previous investigations[32]. However, the proteins in the microplaques are clearly not fully alpha helical when compared to standards such as keratin, which possesses dominant alpha helical coiled coil structure (Supplementary Fig. 9). Additionally, in microplaque spectra we observe a shoulder at ~1590 $cm^{-1}$ which could correspond to $C_4=C_5$ stretching of the imidazole ring bound to a metal ion (Figs. 1D-E)[33], consistent with previous findings[14]. These differences in the spectra between plaque vesicles and microplaques make sense considering plaque vesicles contain many unstructured plaque proteins while microplaques are enriched in mefp-12 (Fig. 1D). Although unrecognized at the time, published Raman spectra from induced plaque proteins in the secretory ducts of mussel foot also suggest the presence of $\alpha$-helical character based on similar spectral features[9].

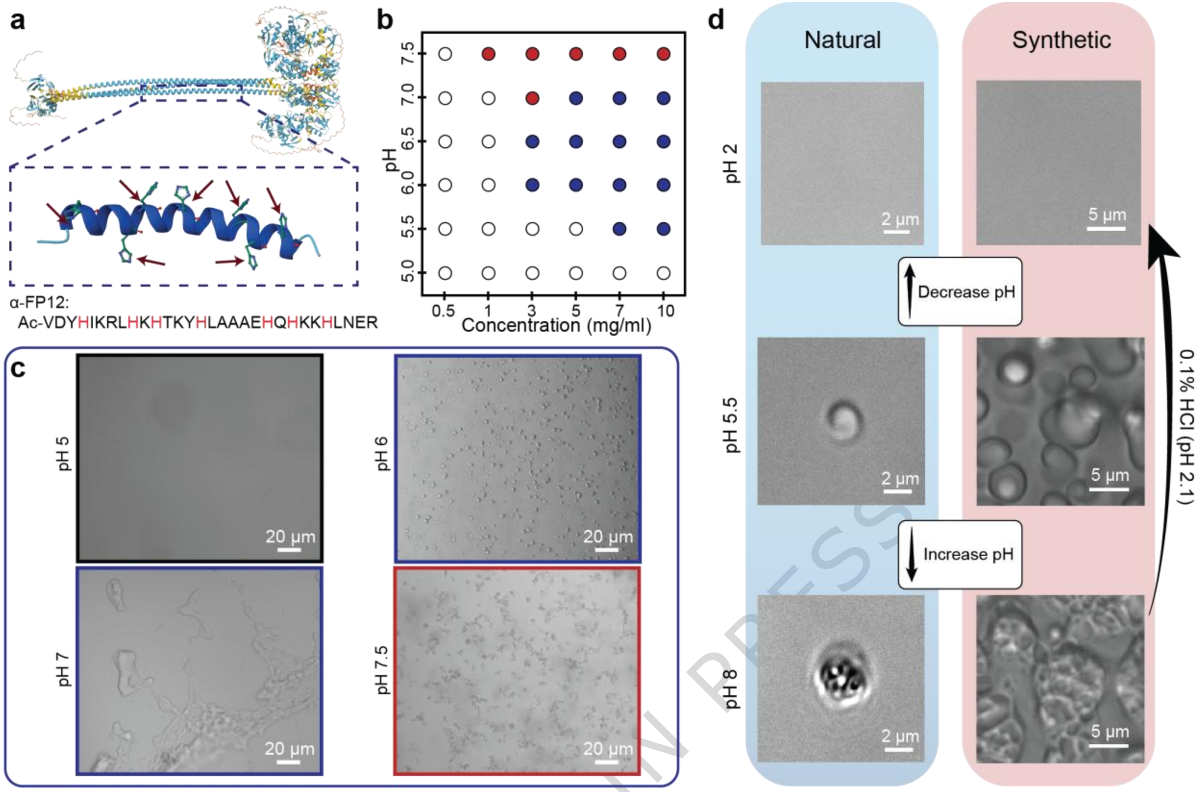

**Figure 4. LLPS and solidification of mefp-12 $\alpha$-FP12 peptide. a** A histidine-rich peptide ($\alpha$-FP12) was designed based on sequence from the predicted CC region of mefp-12. Red arrows show positions of histidine on the AlphaFold3 structural model. **b** Phase diagram showing phase separation (blue), aggregation (red), and solution (white) as a function of pH and peptide concentration at 1M NaCl and a 3:1 His:Zn$^{2+}$ ratio. **c** Light microscopy images showing pH-dependent coacervation and aggregation of $\alpha$-FP12. **d** Comparison showing similarity of $\alpha$-FP12 coacervation and solidification with microplaque formation from extracted plaque vesicles (**c, d:** *N* = 3 from 3 different samples).

### *$\alpha$-helical mefp-12 peptides exhibit native-like Zn- and pH-dependent self-assembly via LLPS*

To further investigate the predicted conformation, metal binding, and potential function of the predicted central helical domain of mefp-12, we synthesized a 30 amino acid peptide ($\alpha$-FP12) with a sequence pulled from the putative histidine-rich alpha helical region (Fig. 4A). Given that plaque vesicle proteins are stored as fluid condensates, we explored the LLPS behavior of $\alpha$-FP12 under a range of relevant conditions – including peptide concentration, pH, salt concentration, and histidine-binding transition metal ions (Zn, Cu, and Ni). As shown in the phase diagram and optical microscopy images in Figs. 4B and 4C, under pH conditions at and slightly below the $pK_a$ of histidine (~6.5) and above concentrations of ~3 mg/ml, $\alpha$-FP12 underwent LLPS, forming small fluid droplets that coalesced and spread over the glass surface (Supplementary Fig. 10 and Supplementary Movie 1). Importantly, LLPS required at least 500 mM NaCl and was entirely zinc-dependent, only occurring in the presence of $Zn^{2+}$ molar ratios of at least 1 $Zn^{2+}$:3 His and not with $Cu^{2+}$ or $Ni^{2+}$ ions. Notably, raising the pH above the $pK_a$ of histidine following coacervation resulted in the solidification of the $\alpha$-FP12 condensate droplets, which spontaneously formed porous solids that strongly resemble the microplaques formed during rupture of native plaque vesicles (Fig. 4D). This is remarkable considering that native vesicles contain all ten plaque proteins found in the secretory vesicles, while the peptide is only a 30 amino acid segment selected from just one of the ten proteins. At higher concentrations, the $\alpha$-FP12 peptide forms large condensates of hundreds of microns that spread over the glass surface and can also be induced to form large open cell porous solids resembling native mussel glue by increasing pH above 8 (Figs. 5A-B and Supplementary Movie 2).

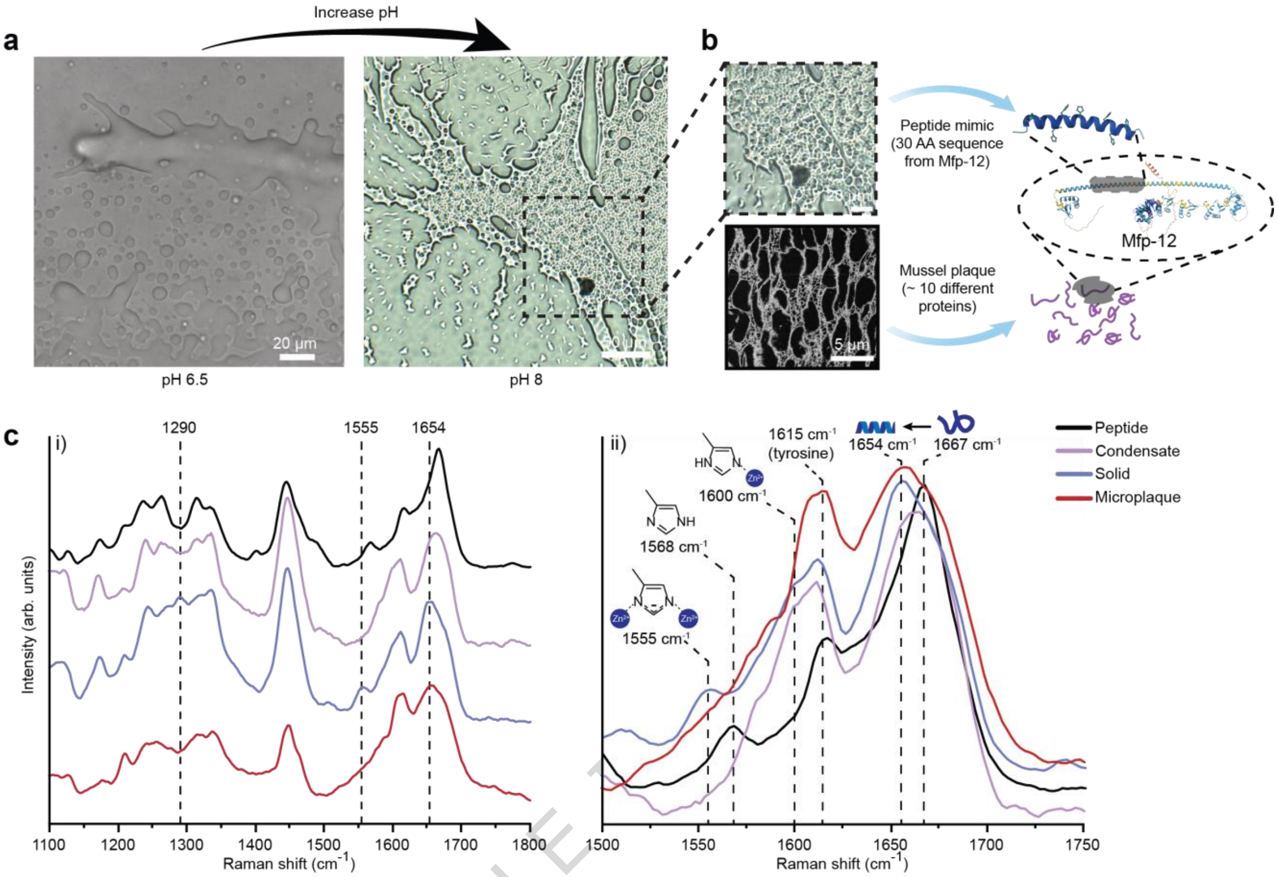

**Figure 5. Structural and conformational transitions during mefp-12 $\alpha$-FP12 peptide condensate solidification. a** Light microscopy image of large $\alpha$-FP12 condensates undergoing pH-triggered solidification into a porous solid that resembles native plaque structure. **b** Zoomed image of inset from panel A, comparing the synthetic solid to an SEM section of the native byssus plaque showing similar microporous structure (**a, b:** $N$ = 3 from 3 different samples). **c** Raman spectra between 1100-1800 cm$^{-1}$ (i) acquired from $\alpha$-FP12 peptide solution (black), condensate droplet (purple), and solid (blue) compared to a microplaque formed from a plaque secretory vesicle (red). Panel (ii) shows the amide I region from (i) between 1500-1750 cm$^{-1}$ , highlighting secondary structure and histidine-metal coordination peaks.

To examine the role of conformation and metal binding in phase separation behavior, confocal Raman spectra were acquired from $\alpha$-FP12 condensates (pH 6.5), which may indicate partial alpha helical structure, but mostly random coil, with the amide I band shifting to lower wavenumbers (~1660 $cm^{-1}$) compared to the pure peptide amide peak at 1667 $cm^{-1}$ (Figs. 1E and 5C) The peak for non-coordinated histidine at 1568 $cm^{-1}$ observed in the pure peptide solution, shifts to ~1600 $cm^{-1}$ with $ZnCl_2$ at pH 6.5, indicating His-Zn coordination, although this peak is overlapping slightly with the ring vibration of tyrosine at ~1615 $cm^{-1}$ (Figs. 1E and 5C). To verify this assignment, measurements of condensates formed in $D_2O$ were performed, showing expected peak shits for a His-Zn vibrational mode at pD 6 (Supplementary Fig. 11)[33]. Thus, we conclude that Zn- and pH-induced coacervation of $\alpha$-FP12 is associated with formation of partial $\alpha$-helical structure and His-Zn metal coordination interactions.

Raman measurements were then performed on $\alpha$-FP12 condensates that were solidified under seawater pH forming porous structures. Spectra from the porous solids showed clear enhancement of $\alpha$-helical amide I and III signatures[32], but also indicated an unexpected change of the metal coordination mode to a doubly deprotonated histidine imidazolate side chain that bridges two Zn ions, based on characteristic peaks at 1290 and 1555 $cm^{-1}$ (Figs. 1E and 5C)[33]. The presence of the Raman signature for the metal-bridging imidazolate ring of histidine is quite unusual to observe at pH 8 given the extremely high $pK_a$ of the second His proton ($pK_a$ ~11-14)[34]. However, this binding mode has been reported previously at physiological pH in the active site metal center of the redox enzyme superoxide dismutase, which possesses a doubly deprotonated histidine residue bridging Cu and Zn ions[35,36]. Additionally, similar Raman peaks for metal bridging histidine imidazolates have been reported in amyloid-$\beta$ fibrils associated with Alzheimer's disease[37] and in mussel-inspired materials produced from histidine-enriched peptides[38-40]. Thus, the internal environment within certain protein folds may favor imidazolate metal bridging, even though this is unlikely to occur in solution phase below pH 11 with pure histidine[34]. While the solidified $\alpha$-FP12 remained stable on the surface indefinitely and persisted upon resubmerging it in solutions above pH 6 (Supplementary Movie 3), it was easily dissolved either by lowering the pH below 6 or by adding EDTA to the solution (Fig. 4D and Supplementary Movies 4 and 5). These observations highlight the key role of histidine-Zn metal coordination interactions in providing stability to the material.

### *Investigation of structural and phase separation behavior by NMR spectroscopy*

In addition to Raman spectroscopy, the physical and biochemical driving forces of $\alpha$-FP12 self-assembly was subjected to additional scrutiny by combining both solution and solid-state nuclear magnetic resonance (NMR) spectroscopies (Supplementary Table 2). First, solution NMR, combining both high field magnet (800 MHz) and cryoprobe, enabled the detection and complete $^{1}H/^{13}C$ assignment (Supplementary Fig. 12, Supplementary Table 3) of the peptide conformation in solution within the range of concentration relevant for this study (*i.e.* from 1mg/mL (265 µM) to 10 mg/mL (2.7 mM)) (Supplementary Fig. 13). Using CSI 3.0[41] and TALOS-N[42,43] NMR secondary structure prediction tools, the peptide in water under acidic conditions (pH 4.3) is consistent with a random coil conformation within this range of concentration, which fits Raman spectroscopic measurements. Exploring pH as a key parameter, the peptide does not show conformational changes in the range from pH 3.0-12.6 in the absence of zinc. However, we detected the changing protonation state of specific amino acids (Supplementary Fig. 14), allowing us to confirm that the His residues in the peptide have an average $pK_a$ of 6.2 (Supplementary Fig. 15, Supplementary Table 4), matching literature values[44,45] and notably, the pH at which coacervation occurs. The narrow distribution of His $pK_a$ further indicates that, without zinc ions, the peptides are likely disordered as a secondary structure would affect local His protonation since they are homogeneously distributed along the peptide sequence.

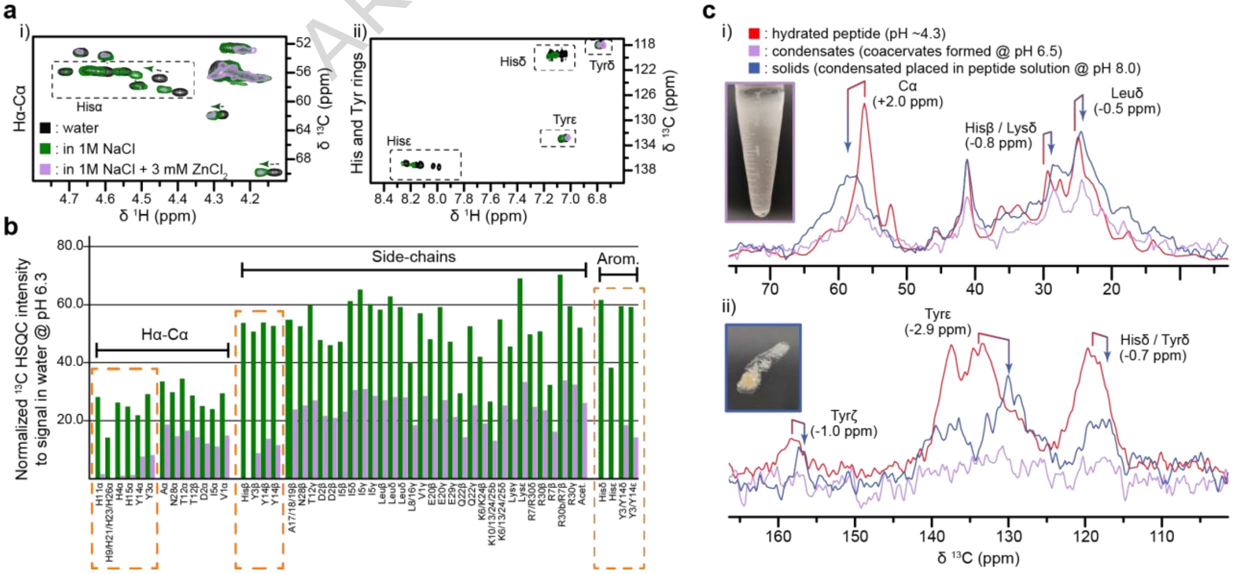

**Figure 6. Characterization of peptide coacervates and solids by NMR. a** $^{1}H$-$^{13}C$ HSQC solution NMR of $\alpha$-FP12 peptide Hα-Cα backbone (left) and aromatic sidechains (right) in water (black spectra), 1M NaCl before (green spectra) and after (purple spectra) addition of $Zn^{2+}$ ions at pH 6.5. **b** Peak integration of $^{1}H$-$^{13}C$ HSQC spectra in 1M NaCl before (green) and after (purple) addition of $ZnCl_2$. Tyr and His sidechain resonance shifts and signal loss suggest that aromatic residues play a key role in coacervate formation or stabilization. **c** Solid-state NMR showing transition of $\alpha$-FP12 peptide solution under acidic conditions (red), to coacervates at pH 6.3 (purple), and toward alpha-helical structure in the solid phase with clear downfield shift of the Cα in basic conditions (blue). Low signal coming from the coacervate indicates intermediate molecular dynamics, making it hard to detect by both solution and solid-state NMR.

With this baseline analysis in hand, we next investigated the effect of salt and ions at different pH using solution NMR. High salt concentrations (0.5 - 1 M NaCl) showed only limited effect on the peptide conformation (a few peaks shifted downfield due to overall difference in solvation or H-bonding[46] (Supplementary Fig. 16)). Consistent with Raman analysis, solution NMR analysis showed only weak secondary structure in the solution and condensate phases (Fig. 6A and Supplementary Figs. 17A-B). Unsurprisingly, condensate formation decreased overall spectra intensity – however, precise quantification showed that specific amino acids are more affected by the coacervate formation than others. Indeed, specific signals corresponding to histidine and tyrosine side chains decreased significantly more in condensates vis-à-vis solutions compared with any other amino acids (Fig. 6B, Supplementary Figs. 17C-D and 18). This indicates that the relaxation rates of histidine and tyrosine, in particular, have been affected, likely suggesting direct involvement in driving coacervate stabilization through transient interactions, as previously identified in histidine-rich squid beak proteins[47,48].

Solid-state NMR, while displaying a lower resolution, allows us to detect more rigid molecules and therefore is a powerful method to investigate the $\alpha$-FP12 solids formed under basic pH conditions. Using high resolution spectra from solution NMR measurements for reference, we partially assigned resonances from the ssNMR spectra, showing a good agreement between peptide in solution and 30% w/w hydrated peptide in ssNMR rotor (Supplementary Fig. 19). Comparing $\alpha$-FP12 in solution at pH 4.3 and in the fluid condensate phase at pH 6.5, only few resonance shifts are detected. It is worth mentioning that the intermediate dynamics of fluid condensates make it hard to detect by both solution and solid-state NMR (Supplementary Fig. 20 A-D). Interestingly, when condensates self-organize into porous solids at pH 8.0, the ssNMR signal is significantly improved, even showing clear Cα resonances shift indicative of increased $\alpha$-helical structure, together with His and Tyr side-chains resonance shifts, further confirming that these amino acids have tightly interacting side chains in the solid phase (Fig. 6C and Supplementary Figs. 20E-F). Notably, the overall poor signal-to-noise ratio of the ssNMR spectra indicates the intermediate molecular motion at play in the coacervate and subsequent solid.

Overall, our Raman and NMR spectroscopic investigation provides strong evidence that $\alpha$-FP12 undergoes zinc-dependent LLPS that involves both histidine and tyrosine residues. Moreover, solidification occurs above the $pK_a$ of histidine through formation of Zn-stabilized $\alpha$-helical CCs that spontaneously self-assemble into a porous network at basic pH.

## Discussion

### *Revisiting and revising the DOPA-centric archetype of mussel adhesion*

The findings of this study challenge the long-held DOPA-centric paradigm of mussel adhesion demonstrating convincingly that His-rich mefp-12 is an important and evolutionarily conserved glue component that plays a key role in the pH-responsive formation of the micro- and nanoporous network and that provides structural integrity to the plaque adhesive under mechanical loading. Indeed, our peptide studies suggest that the mefp-12 CC domain drives pH-triggered and zinc-dependent phase separation, as well as subsequent solidification of the plaque – in line with the proposed pH-dependent assembly of the native plaque. While future studies focusing on the native protein in its entirety (e.g., via recombinant expression or purification) will be important to further confirm its role within the plaque, the current findings indicate a chemically regulated capacity for self-assembly and solidification that is programmed into the primary sequence of the His-rich CC domain. In this modified model of mussel glue fabrication (Fig. 7), we posit that pH-triggered $Zn^{2+}$ binding by mefp-12 initiates the conformational transition to $\alpha$-helical structure and association of these proteins into a porous network, excluding certain DOPA-rich adhesive plaque proteins in the vesicles, which remain as fluid condensates within the pores of the cured scaffold (Fig. 7)[14]. As previously proposed, the connectivity of the open-cell porous network of the plaque likely provides a means of transporting the fluid adhesive protein to the surface to replenish damaged adhesive contacts and allow long lasting substrate adhesion[18].

Solidification of protein LLPS droplets is typically associated with formation of beta crystalline amyloid conformation, which exists as an energy minimum in the protein folding landscape[49,50]. Thus, the observation that the $\alpha$-FP12 peptide fluid condensates, and presumably mefp-12, reach an energy minimum in the arrested state consisting of metal stabilized $\alpha$-helical coiled coils is noteworthy and perhaps functionally relevant. CCs are found in numerous biological materials, often in the form of intermediate filaments like keratin, vimentin, and lamin[51], providing the propensity for increasing material toughness and damping in cyclic loading, due to rupture of sacrificial hydrogen bonds along the helix and unfolding of the protein chain reaching strains up to 150%[52]. Importantly, in most CC-based materials this unfolding is completely reversible – when the force is removed, the CC refolds, providing elastomeric mechanics and high mechanical hysteresis[32,53]. Furthermore, His-metal cross-linking can provide additional mechanical enhancement of folded protein domains, as reported for other byssus proteins[29,54], globular domains[55], and bioengineered CCs[40,56]. This is relevant in the context of the crashing waves that batter mussels, for which mechanical hysteresis and toughness are crucial parameters for survival[57]. Notably, the fibrous core of the thread is also well-known to use His-Zn coordination as an assembly trigger and as a sacrificial cross-link for providing thread toughness and self-healing capacity[2,29,30]. It is tempting to further speculate that the predicted Zn-finger-like domains of mefp-12 may provide additional toughening capacity. Indeed, there are numerous examples in nature of tandemly repeated globular domains that function in such a capacity –notably, the Ig domains of the massive muscle protein titin[58]. However, verifying this hypothesis requires further study.

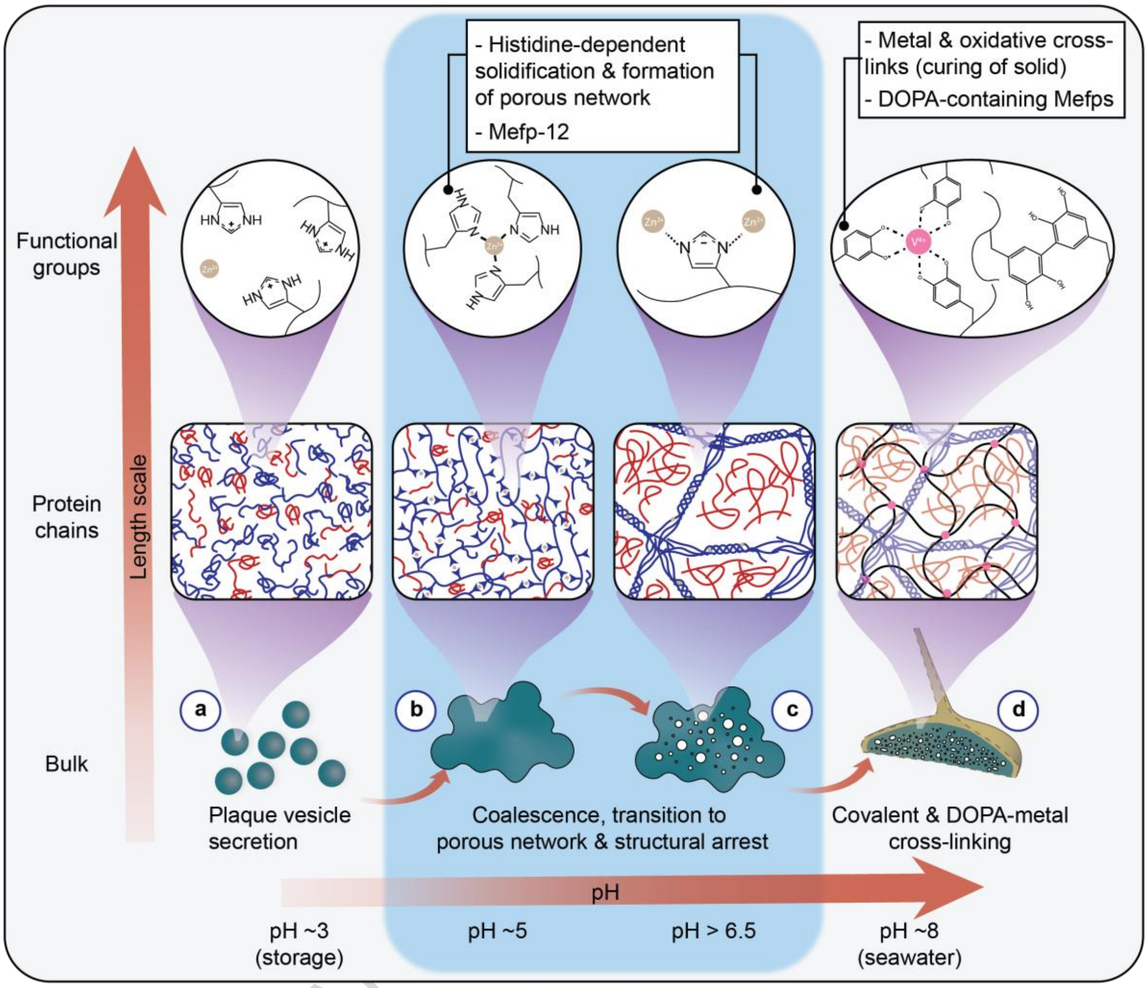

**Figure 7. Illustrative model of proposed mechanism of liquid-to-solid phase transition during porous plaque scaffold formation.** Schematic showing the proposed pH- and metal-dependent structure and metal coordination changes occurring during plaque formation, resulting in the final open-cell network assembly. Proteins destined to form the solid plaque scaffold appear blue, while adhesive proteins appear red. **a** Mefp-12 within intact vesicles are stored at acidic pH and are fully protonated, unable to bind metal ions. **b** Upon secretion and gradual increase in pH, vesicle contents coalesce and are held together by His-zn metal coordination, but mefp-12 remains mostly unstructured. **c** Under basic conditions nearing the pH of seawater, spontaneous phase separation and solidification of the plaque is driven by CC formation of mefp-12 stabilized by histidine

imidazolate coordination bridging two Zn ions. During this process, the proteins comprising the solid porous scaffold (blue) – notably, mefp-12 – are segregated from the adhesive proteins (; e.g., mefp-3, mefp-5, and mepf-6), which remain as condensates in the pores (red) **d** Vanadium ions are secreted and coordinate with DOPA-containing proteins adding a second, stronger metal-coordination network, further toughening the plaque scaffold.

While DOPA-metal coordination with plaque proteins has also been proposed as a metal-based cross-linking strategy in plaque formation[4,9], these are not mutually exclusive glue curing mechanisms. We posit that histidine-Zn cross-linking offers several additional benefits for glue fabrication and function. Indeed, it seems plausible that the use of both His-Zn and DOPA-V/Fe cross-linked networks together may further enhance plaque toughness (Fig. 7). For example, double network hydrogels consist of two interpenetrating polymer networks, which are stabilized by orthogonal cross-linking chemistries with differing strengths [59,60]. The weaker sacrificial network ruptures prior to the stronger network, dissipating significant mechanical work, substantially enhancing material toughness. Histidine-metal bonds possess a single molecule breaking force that is approximately one-third of DOPA-metal bonds[55,61], which means they might act in a sacrificial manner within the proposed double network of the plaque, just as they act as sacrificial bonds with the collagenous core of byssal threads to enhance toughness and provide self-healing capacity[29]. Moreover, histidine does not suffer from the well-known tendency of DOPA to oxidize, which can induce formation of non-reversible covalent cross-links over time[15,62]. While these speculations remain to be validated experimentally, the insights extracted in this study provide a much deeper understanding of the mechanism underlying the formation and function of this biological glue, which in turn imparts further inspiration for next generation bio-inspired adhesives, coatings, and hydrogels with potential for biomedical and technical applications.

## Methods

### *Ethical statement*

This research complies with all relevant ethical regulations for testing and research of *Mytilus edulis* in Canada.

*Mariculture & Plaque Vesicle Isolation*

Mussels (*Mytilus edulis*) farmed on the Atlantic coast of Canada (Prince Edward Aqua Farms, PEI, Canada) were maintained in an aquarium at 12-15 °C in artificial seawater (Fluval Sea, USA; containing Ca, K, Mg and Sr) adjusted to 3%. Only adult specimens were used; sex was not determined, as it was not relevant to the study. Extracellular plaque vesicles were extracted and isolated from mussel foot tissue following a previously published protocol[17]. To summarize, 0.5 g of gland tissue was dissected from mussel feet and homogenized in a chilled glass homogenizer (Wheaton) in 5 mL of a 150 mM citrate-phosphate buffer solution (pH 5.5) containing 500 mM sucrose, 150 mM EDTA and 5 mM ascorbic acid. The resulting crude homogenate was combined 1:1 with a 30% OptiPrep solution (Sigma), filtered through a 40 µm nylon cell strainer and layered onto a 30/27.5/25/22.5/20/17.5% discontinuous OptiPrep gradient. After centrifugation for 200 minutes at 4000*g*, 4 °C, the 27.5/25% interface (containing plaque vesicles) was collected. To remove excess OptiPrep prior to downstream experiments, the vesicle solution was combined 1:1 with homogenization buffer, centrifuged at 500*g* for 1 hour to pellet vesicles, followed by resuspension in 100-200 µL of fresh homogenization buffer.

*Gel Electrophoresis & Western Blots*

Plaque vesicles were centrifuged at 15,000g for 15 minutes and resolubilized in 30 µL of 0.1% HCl, causing them to rupture, forming a solution of plaque proteins. This solution was then combined with 10 µL of 4x Laemmli sample buffer, heated at 90 °C for 5 minutes, and run on a discontinuous 15% SDS gel (Laemmli Tris-glycinate electrode buffer protocol). Coomassie Brilliant Blue (Bio-Rad) was used to stain and visualize bands. For Pauly staining, bands were blotted onto nitrocellulose membranes. Pauly staining was carried out as described previously[23], by incubating a blotted nitrocellulose membrane in a 20 mL solution of equal parts 1) 5% w/v sodium nitrite, prechilled, and 2) 0.9 g of sulfanilic acid dissolved in 100 mL of 1M HCl for 5 minutes under gentle shaking. 20mL of 10% w/v sodium carbonate is then added until orange coloration of bands is achieved.

For microplaque compositional investigation, microplaques were formed by combining isolated plaque vesicles with Milli-Q water at a ratio of 1:10 on a glass slide and left to rest for 20 minutes. The solution was removed, leaving behind microplaques adhered to the glass surface, which were subsequently resolubilized by incubation in 0.1% HCl. The resulting solution was run on a 15 % gel as described above and visualized by use of the Silver Stain Plus kit (Bio-Rad) due to the very low concentration of proteins.

### *Rapid Amplification of cDNA Ends (RACE)*

Gene-specific primers (Supplementary Table 5) were used to amplify overlapping 5′ and 3′ fragments from RACE libraries prepared from *M. edulis* foot tissue. RACE PCR amplicons were subsequently cloned into pGEM-T (Promega) using standard TA-cloning methods, and cloned fragments were sequenced by standard Sanger chemistry. Genbank Accession: PV698367.

### *In situ hybridization*

*In situ* hybridization (ISH) was carried out as described previously[63,64]. In brief, three mussel feet were dissected from live mussels, with their RNA extracted using a TRIzol Reagent kit (Thermofisher). Synthesis of cDNA by reverse transcription of the extracted RNA was carried out with a Reverse Transcription kit (Roche), with double stranded DNA templates amplified by PCR using the Q5 High-Fidelity DNA Polymerase kit method. Primers were designed with Open Primer 3 (https://bioinfo.ut.ee/primer3/, optimal probe length 700-900 bp). Purification of the resulting PCR products for probe synthesis was done with Wizard SV Gel and PCR clean-up system kit (Promega). A DIG RNA Labelling kit (Roche) with T7 RNA Polymerase and DIG-dUTP was then used for Digoxigenin (DIG)-labelled RNA probe synthesis, which were used on transverse sections of a mussel foot at a concentration of 0.2 ng/µL. Detection was performed by using antidigoxigenin-AP Fab fragments (Roche) at a 1:2000 dilution, coupled with the NBT/BCIP system (Roche) at a 1:50 dilution at 37 °C for signal development until satisfactory tissue coloration was achieved form the resulting precipitate. Controls without probes and without antibodies were also performed on the tissue sections. Imaging was done on an upright

Axioscope.A1 polarized light microscope (Zeiss) with a 5× objective (Zeiss) coupled with a 6-megapixel Axiocam 506 color camera (Zeiss).

### *Secondary Structure, Multimerization and Metal Binding Predictions*

AlphaFold3[65] and Chai[66] were used for monomer, multimer, and metal binding secondary structure predictions. The WaggaWagga algorithm[26] was used to further confirm coiled coil formation. All predictions were performed on their respective freely available web servers (https://alphafoldserver.com/; https://lab.chaidiscovery.com/dashboard; https://waggawagga.motorprotein.de/). Monomer and dimer structures were predicted on both AlphaFold3 and Chai, while trimers and tetramers were solely predicted on AlphaFold3 due to length restrictions on the Chai platform. For image generation & visualization, CIF files for the predicted structures were uploaded to the online version of Mol* (https://molstar.org/viewer/).

### *Cross-Species Sequence Analysis*

All sequences from the other mytilid species compared to mefp-12 were found on the NCBI Protein Databank, with accession numbers available in Supplementary Fig. 1. Sequence alignment and highlighting was performed in the BioEdit[67,68] sequence alignment editor software using the ClustalW Multiple Alignment accessory application available within the BioEdit software to align all available Mfp-12 sequences.

### *Peptide Coacervate Formation & Solidification*

The 30 amino acid $\alpha$-FP12 peptide (VDYHKRLHKHTKYHLAAAEHQHKKHLNER) used in this study was synthesized by Biomatik Corporation with an acetylated N-terminus. For coacervation studies, the peptide was dissolved in a solution of 25 mM MES buffer (Sigma), with pH adjusted with concentrated HCl or NaOH, and ionic strength adjusted to 0.5 M or 1 M with NaCl. Coacervation was induced by mixing this peptide solution with stock solutions of zinc chloride (Sigma) at a 9:1 ratio to give a final solution with a ratio of 3 histidine residues to 1 zinc ion. For pH-dependent phase separation and solidification experiments, a 1 µL aliquot of coacervate droplets was allowed to settle onto the surface of a glass slide. A 20 µL volume of 25mM PIPPS buffer (Sigma) at pH 8 and 0.5 M ionic strength was pipetted over the 1 µL droplet triggering pore formation and solidification. The solution was subsequently washed two additional times with 20 uL aliquots of the PIPPS solution to ensure pH homogeneity. For further dissolution experiments**,** solidified peptides were then air dried prior to being resubmerged in 20 µL of PIPPS solution (pH 8, Supplementary Movie 3) or 0.1% HCl in Milli Q water (pH 2.05, Supplementary Movie 4). Images and videos of droplet settling and solidification were taken on an Axio Observer inverted microscope (Zeiss) equipped with a 40x air objective (Zeiss) an Axiocam 705 mono camera (Zeiss).

### *Raman Spectroscopy*

Raman spectra of samples were collected on an Alpha300R confocal Raman microscope (Oxford Instruments) coupled with a green laser (532 nm) and either a 50x air (Zeiss, numerical aperture = 0.8) or 100x oil-immersion (Zeiss, numerical aperture = 1.25) objective. Spectra were taken at a laser power of 12 mW and an integration time of 3 s per point. Scattered light was collected with a thermoelectrically cooled CCD detector (Andor). WITec's ControlFIVE and ProjectFIVE software were used for spectrum collection and processing, respectively. Spectral processing consisted of background subtraction, cosmic ray removal and smoothing. Spectra were then plotted using OriginPro software.

### *Chemical Fixation and Embedding*

Fixation of native plaques (N = 2) was carried out for 1 h at 4 °C in 2.5% glutaraldehyde and 1.5% paraformaldehyde in 0.1 M cacodylate buffer pH 7.4. Samples were rinsed 3× 10 min in 0.1 M cacodylate buffer at 4 °C before post fixation with 1% OsO4 for 1 h. A second rinsing step in distilled $H_2O$ (3 × 5 min at 4 °C) was followed by dehydration in acetone (50, 70, 90%, 3× 100%) for 10 min each step at room temperature. Plaques were embedded in epoxy (Epon 812 substitute, Sigma-Aldrich, # 45359) at 65 °C over 2 days.

### *FIB-SEM of Native Byssus Plaque*

A resin block containing byssus plaque samples was polished to expose the plaque at the block surface and sputter-coated with three carbon layers of ~5 nm each and one platinum layer of ~5-10 nm. The sample was then transferred to the Zeiss Crossbeam 540 (Zeiss, Germany) and a trench was milled into the sample surface for SEM imaging using an acceleration voltage of 30 kV and a FIB current of 65 nA. The cross section was then finely polished with a 7 nA FIB probe at 30 kV. Thin serial slices were removed by FIB milling (700 pA, 30 kV, 40 nm thickness). The sample was imaged after each milling step by SEM using a backscattered electron detector at an acceleration voltage of 2 kV. Resulting image resolution was 1024 x 768 pixels with a lateral pixel size of ~20 nm. Image recording was done using line averaging (N = 22) and a dwell time of 200 ns.

Backscattered (BSE) electron images of plaque samples were processed in Dragonfly 2024.1, with images registered by using the Sum of Square Differences (SDD) method with a medium translation and subsequently cropped. Denoising was achieved by using the convolution filter (3D, level 7, circle). The plaque micro- and nanopores were segmented with the Dragonfly 2024.1 Segmentation Wizard and exported to a normal mesh (sampled 4 x 4 x 4).

*NMR Spectroscopy*

For solution NMR analysis, lyophilized α-FP12 peptides were dissolved at 0.5/1 %w/v (1.3/2.6 mM) in 1M NaCl water (containing 10 % deuterated water) solution and then pH was adjusted using NaOH and HCl. Overall, salt significantly decreases signal-to-noise of cryoprobe-collected data (by increasing sample conductivity and affecting 90° pulses[69]), but using 3 mm NMR tubes instead of 5 mm significantly decrease this artifact. When adding ions, for instance to form coacervates, pH was adjusted before adding ion solutions. To reach a final 3:1 His:$Zn^{2+}$ stoichiometry, 1 volume of a 10× concentrated ion solution was added to 9 volumes of peptide solution. Doing so, the effect of ion stock on the final pH solution was limited considering that $ZnCl_2$ is not soluble at high pH.

All solution NMR samples were performed at least twice acquired at 25°C on an 800 MHz NMR Avance III HD Bruker NMR spectrometer equipped with a TXI triple resonance cryoprobe. Samples were referenced to Sodium trimethylsilylpropanesulfonate (DSS) at 0 ppm (for both $^{13}C$ and $^{1}H$ referencing)[70]. $^{15}N$ referencing was performed indirectly simply using $^{15}N$ gyromagnetic ratio and 1H chemical shift correction (Topspin SR parameter)[70,71]. Temperature was calibrated to 25 °C (with margin of error of 0.1 °C) *via* a methanol thermometer[72]. TopSpin 4.4.0 and MestReNova 15.0.1 software were used to plot, process, analyze and assign spectra. Spectra were automatically phased baseline corrected using Topspin software. For consistent peak integration and quantification, receiver gain was kept constant for all NMR acquisitions.

Peptide complete $^{1}H/^{13}C/^{15}N$ is summarized on Supplementary Table 3. This assignment was performed using $^{1}H$-$^{1}H$ COSY/TOCSY/NOESY, $^{1}H$-$^{13}C$ HSQC and $^{1}H$-$^{15}N$ HSQC experiments included in the Topspin software package. Typical acquisition parameters are summarized in Supplementary Table 4. Due to low abundance and sensitivity of $^{15}N$ nuclei, 1H-15N HSQC with 25% non-uniform sampling (NUS) was used to obtain an 8-hour experiment. The same experiments were used to determine specific amino acids involved in transient binding toward coacervate formation. By integrating the different peaks, we quantified the residues tightly bound in coacervates as the residues with the most intensity decrease.

Once fully assigned, NMR chemical shift changes were monitored as function of pH and fitted to determine pKa using OriginPro 2023 software with the formula below as previously reported[73,74]:

$$(1)\ \delta_{obsv}(pH) = \frac{\delta_H 10^{(pKa-pH)} + \delta_L}{1 + 10^{(pKa-pH)}}$$

With $\delta_{obsv}$ the observed chemical shift, pKa the calculated acid dissociation constant (pKa), $\delta_H$, $\delta_L$the limiting chemical shifts of the totally protonated and deprotonated analyte, respectively.

For samples analyzed by solid-state NMR acquired at 25°C and 15 kHz MAS on a 600 MHz Advance III HD Bruker NMR spectrometer equipped with a Phoenix NMR HXY triple resonance probe at 15, a large amount of coacervates and solid were prepared (30 mg of peptide forming coacervates in 6 mL). Once formed, coacervates slowly accumulate on the glass side of the tube and are carefully scraped down to form a pellet that is subsequently transferred in a 3.2 mm NMR rotor. Due to peptide quantities needed for these experiments, all samples were prepared one time.

## Data Availability

All relevant data generated or analyzed during this study are included in this published article, supplementary information files, and source data files. The mass spectrometry proteomics data have been deposited to the ProteomeXchange Consortium via the PRIDE partner repository with the dataset identifier PXD067305 [https://www.ebi.ac.uk/pride/archive/projects/PXD067305]. Transcriptomic data are available on the NIH BioSample Database (https://www.ncbi.nlm.nih.gov/biosample) with project number PRJNA1225934 [https://www.ncbi.nlm.nih.gov/bioproject/PRJNA1225934]. Protein sequence data is available on the Genbank Protein database with accession number PV698367 [https://www.ncbi.nlm.nih.gov/nuccore/PV698367]. All the NMR data generated in this study have been deposited in the Zenodo database under the DOI 10.5281/zenodo.18271247. NMR resonance assignment available in supplementary tables have been uploaded to the BMRB database with Accession Number 53425 [https://bmrb.io/data_library/summary/?bmrbId=53425]. Source data are provided with this paper.

## Acknowledgements

We thank T. Sprules at the McGill Chemistry Characterization (MC2) facility and A. Arnold at the UQAM Nanoqam NMR facility for support with NMR experiments, as well as L. Taylor from the MUHC Proteomics and Molecular Analysis platform at McGill for MS/MS proteomics support. MJH acknowledges funding from the Natural Sciences and Engineering Research Council of Canada (NSERC Discovery Grant RGPIN-2024-04221), a Canada Research Chair award (CRC Tier 2 950−231953), and the Swiss National Science Foundation (SNSF Sinergia Grant CRSII5−216558). DJJ was funded by the DFG (JA 2108/8-1 project number 528314512). PF was funded by a FNRS PDR project (T.0088.20).) ED was supported by a FRIA doctoral fellowship from the Fund for Scientific Research of Belgium (F.R.S.-FNRS). FJ was funded by the Max Planck Society.

## Contributions

M.D.R. and M.J.H. conceived the idea. M.J.H. supervised the work. M.D.R., A.P., M.J.R-R, E.D., F.J., and D.J.J. performed the experiments. M.J.H., M.D.R., A.P., M.J.R-R, P.F. and D.J.J. analyzed the data. M.J.H., M.D.R. and A.P. co-wrote the paper. All authors discussed the results and commented on the manuscript.

## Competing interests

The authors declare no competing interests.

## Figure Legends

**Figure 1. Self-assembly of porous mussel glue. a** Mussels attach to surfaces using byssal threads, which terminate at the plaque – a porous underwater glue made of different proteins precisely localized in the plaque. The plaque comprises a solid scaffold and fluid condensate glue proteins trapped within the pores. **b** Byssal threads are produced by a secretory organ known as the foot. Plaque proteins are stored in vesicles within the foot plaque secretory gland as fluid condensate droplets, which are secreted into the distal depression in the foot where they begin to solidify. **c** When they burst, purified plaque vesicles undergo salt- and pH-dependent liquid-liquid phase separation (LLPS) and subsequent solidification, forming a porous microplaque. **d** Microplaque-specific proteins are enriched in histidine, and Raman spectroscopy suggests the presence of histidine metal coordination cross-linking and partial alpha helical secondary structure in microplaques, based on peak positions denoted by dashed lines. **e** Schematic of pH-dependent histidine deprotonation and metal binding with associated characteristic Raman peaks noted.

**Figure 2. Localization and sequence elucidation of the histidine-rich adhesive protein mefp-12 in *Mytilus edulis*. a** Plaque vesicles contain the histidine rich protein mefp-12, confirmed with Pauly staining of SDS gels (**a**: *N* = 2 gels from 2 specimens). **b** Sequence of mefp-12 (from *Mytilus edulis*) with signal sequence underlined in black, histidine residues highlighted in red, and MS/MS confirmed peptides boxed (Genbank Accession: PV698367**). c** *In-situ* hybridization (ISH) shows that mefp-12 is produced exclusively in the plaque secretory gland corresponding to the green regions of the

illustrated foot cross-sections (blue and red regions correspond to the core and cuticle glands, respectively).

**Figure 3. Analysis of mefp-12 sequence homology and *in silico* predicted structure, oligomerization, and metal-binding. a** Comparison of mefp-12 sequences from other mytilid mussels with dots indicating conserved amino acids across species and dashes indicating gaps, highlighting the strong homology (notably in repetitive globular domains highlighted in green and the central helical domain highlighted in lavender). Conserved histidine residues within the helical domain are boxed in red. A 6th globular domain, contoured in red, is present exclusively in *M. edulis* and *M. galloprovincialis*. **b** AlphaFold3 structural prediction of Mefp-12, with repeated globular domains highlighted. **c** Monomeric to tetrameric conformational structures predicted for mefp-12, highlighting oligomerization and Zn-binding of CC domain ($Zn^{2+}$ appears as orange spheres, confidence < 50%).

**Figure 4. LLPS and solidification of mefp-12 $\alpha$-FP12 peptide. a** A histidine-rich peptide ($\alpha$-FP12) was designed based on sequence from the predicted CC region of mefp-12. Red arrows show positions of histidine on the AlphaFold3 structural model. **b** Phase diagram showing phase separation (blue), aggregation (red), and solution (white) as a function of pH and peptide concentration at 1M NaCl and a 3:1 His:$Zn^{2+}$ ratio. **c** Light microscopy images showing pH-dependent coacervation and aggregation of $\alpha$-FP12. **d** Comparison showing similarity of $\alpha$-FP12 coacervation and solidification with microplaque formation from extracted plaque vesicles (**c, d:** *N* = 3 from 3 different samples).

**Figure 5. Structural and conformational transitions during mefp-12 $\alpha$-FP12 peptide condensate solidification. a** Light microscopy image of large $\alpha$-FP12 condensates undergoing pH-triggered solidification into a porous solid that resembles native plaque structure. **b** Zoomed image of inset from panel A, comparing the synthetic solid to an SEM section of the native byssus plaque showing similar microporous structure (**a, b:** *N* = 3 from 3 different samples). **c** Raman spectra between 1100-1800 $cm^{-1}$ (i) acquired from $\alpha$-FP12 peptide solution (black), condensate droplet (purple), and solid (blue) compared to a microplaque formed from a plaque secretory vesicle (red). Panel (ii) shows the amide I region from (i) between 1500-1750 $cm^{-1}$ , highlighting secondary structure and histidine-metal coordination peaks.

**Figure 6. Characterization of peptide coacervates and solids by NMR. a** $^1$H-$^{13}$C HSQC solution NMR of $\alpha$-FP12 peptide Hα-Cα backbone (left) and aromatic sidechains (right) in water (black spectra), 1M NaCl before (green spectra) and after (purple spectra) addition of $Zn^{2+}$ ions at pH 6.5. **b** Peak integration of $^1$H-$^{13}$C HSQC spectra in 1M NaCl before (green) and after (purple) addition of $ZnCl_2$. Tyr and His sidechain resonance shifts and signal loss suggest that aromatic residues play a key role in coacervate formation or stabilization. **c** Solid-state NMR showing transition of $\alpha$-FP12 peptide solution under acidic conditions (red), to coacervates at pH 6.3 (purple), and toward alpha-helical structure in the solid phase with clear downfield shift of the Cα in basic conditions (blue). Low signal coming from the coacervate indicates intermediate molecular dynamics, making it hard to detect by both solution and solid-state NMR.

**Figure 7. Illustrative model of proposed mechanism of liquid-to-solid phase transition during porous plaque scaffold formation.** Schematic showing the proposed pH- and metal-dependent structure and metal coordination changes occurring during plaque formation, resulting in the final open-cell network assembly. Proteins destined to form the solid plaque scaffold appear blue, while adhesive proteins appear red. **a** Mefp-12 within intact vesicles are stored at acidic pH and are fully protonated, unable to bind metal ions. **b** Upon secretion and gradual increase in pH, vesicle contents coalesce and are held together by His-zn metal coordination, but mefp-12 remains mostly unstructured. **c** Under basic conditions nearing the pH of seawater, spontaneous phase separation and solidification of the plaque is driven by CC formation of mefp-12 stabilized by histidine imidazolate coordination bridging two Zn ions. During this process, the proteins comprising the solid porous scaffold (blue) – notably, mefp-12 – are segregated from the adhesive proteins (; e.g., mefp-3, mefp-5, and mepf-6), which remain as condensates in the pores (red) **d** Vanadium ions are secreted and coordinate with DOPA-containing proteins adding a second, stronger metal-coordination network, further toughening the plaque scaffold.

## References

1 Harrington, M. J., Mezzenga, R. & Miserez, A. Fluid protein condensates for bio-inspired applications. *Nat. Rev. Bioeng.* **2**, 260–278, (2024).

2 Rising, A. & Harrington, M. J. Biological materials processing: Time-tested tricks for sustainable fiber fabrication. *Chem. Rev.* **123**, 2155–2199, (2023).

3 Waite, J. H. & Harrington, M. J. Following the thread: Mytilus mussel byssus as an inspired multi-functional biomaterial. *Can. J. Chem.* **100**, 197-211, (2021).

4 Hwang, D. S. *et al.* Protein- and metal-dependent interactions of a prominent protein in mussel adhesive plaques. *J. Biol. Chem.* **285**, 25850-25858, (2010).

5 Zhao, H., Robertson, N. B., Jewhurst, S. A. & Waite, J. H. Probing the adhesive footprints of mytilus californianus byssus. *J. Biol. Chem.* **281**, 11090-11096, (2006).

6 Zhao, H. & Waite, J. H. Linking adhesive and structural proteins in the attachment plaque of *mytilus californianus*. *J. Biol. Chem.* **281**, 26150-26158, (2006).

7 Zhao, H. & Waite, J. H. Proteins in load-bearing junctions: The histidine-rich metal-binding protein of mussel byssus. *Biochemistry* **45**, 14223-14231, (2006).

8 Lee, B. P., Messersmith, P. B., Israelachvili, J. N. & Waite, J. H. Mussel-inspired adhesives and coatings. *Annu. Rev. Mater. Res.* **41**, 99-132, (2011).

9 Priemel, T. *et al.* Microfluidic-like fabrication of metal ion–cured bioadhesives by mussels. *Science* **374**, 206-211, (2021).

10 Krogsgaard, M., Nue, V. & Birkedal, H. Mussel-inspired materials: Self-healing through coordination chemistry. *Chem. Eur. J.* **22**, 844-857, (2016).

11 Zhang, C. *et al.* Mussel-inspired hydrogels: From design principles to promising applications. *Chem. Soc. Rev.* **49**, 3605-3637, (2020).

12 Zhang, X. *et al.* Mussel-inspired fabrication of functional materials and their environmental applications: Progress and prospects. *Appl. Mater. Today* **7**, 222-238, (2017).

13 Priemel, T., Degtyar, E., Dean, M. N. & Harrington, M. J. Rapid self-assembly of complex biomolecular architectures during mussel byssus biofabrication. *Nat. Commun.* **8**, 14539, (2017).

14 Renner-Rao, M. *et al.* Mussels fabricate porous glues via liquid-liquid phase separation of multi-protein condensates. *ACS Nano* **16**, 20877–20890, (2022).

15 Du, C., Rammal, M., Rivard, M. D., Harrington, M. J. & Mauzeroll, J. Mussels put their best “ph”oot forward: Importance of ph in formation of biological and bio-inspired materials. *Adv. Funct. Mater.* **34**, 2409463, (2024).

16 Filippidi, E. *et al.* The microscopic network structure of mussel (*mytilus*) adhesive plaques. *J. R. Soc. Interface* **12**, 20150827, (2015).

17 Renner-Rao, M. *et al.* Mussels fabricate porous glues via multiphase liquid–liquid phase separation of multiprotein condensates. *ACS Nano* **16**, 20877-20890, (2022).

18 Valois, E., Mirshafian, R. & Waite, J. H. Phase-dependent redox insulation in mussel adhesion. *Sci. Adv.* **6**, eaaz6486, (2020).

19 Wilhelm, M. H., Filippidi, E., Waite, J. H. & Valentine, M. T. Influence of multi-cycle loading on the structure and mechanics of marine mussel plaques. *Soft Matter* **13**, 7381-7388, (2017).

20 Rivard, M. D. *et al.* Proteins, processing, and properties of adhesive fluid condensates purified from mussels. *Advanced Functional Materials* **DOI:10.1002/adfm.202523693**, (2025).

21 DeMartini, D. G., Errico, J. M., Sjoestroem, S., Fenster, A. & Waite, J. H. A cohort of new adhesive proteins identified from transcriptomic analysis of mussel foot glands. *J. R. Soc. Interface* **14**, 20170151, (2017).

22 Valois, E., Mirshafian, R. & Waite, J. H. Phase-dependent redox insulation in mussel adhesion. *Science Advances* **6**, eaaz6486, (2020).

23 Sahal, D. *et al.* Specific and instantaneous one-step chemodetection of histidine-rich proteins by pauly's stain. *Anal. Biochem.* **308**, 405-408, (2002).

24 Youssef, L. *et al.* A dynamic biointerface in mussels mediated by a mechanoresponsive intermediate filament-based biopolymer. *In Review*, (2025).

25 Audino, J. A., Serb, J. M. & Marian, J. E. A. R. Phylogeny and anatomy of marine mussels (bivalvia: Mytilidae) reveal convergent evolution of siphon traits. *Zool. J. Linn. Soc.* **190**, 592-612, (2020).

26 Simm, D., Hatje, K. & Kollmar, M. Waggawagga: Comparative visualization of coiled-coil predictions and detection of stable single α-helices (sah domains). *Bioinformatics* **31**, 767-769, (2015).

27 Parry, D. A., Fraser, R. B. & Squire, J. M. Fifty years of coiled-coils and α-helical bundles: A close relationship between sequence and structure. *J. Struct. Biol.* **163**, 258-269, (2008).

28 Kluska, K., Adamczyk, J. & Krężel, A. Metal binding properties, stability and reactivity of zinc fingers. *Coord. Chem. Rev.* **367**, 18-64, (2018).

29 Schmitt, C. N. Z., Politi, Y., Reinecke, A. & Harrington, M. J. Role of sacrificial protein–metal bond exchange in mussel byssal thread self-healing. *Biomacromolecules* **16**, 2852-2861, (2015).

30 Renner-Rao, M., Priemel, T., Anderson, J., Jehle, F. & Harrington, M. J. Multiresponsive liquid crystal collagen guides mussel byssus formation. *Biomacromolecules* **25**, 6038-6049, (2024).

31 Coombs, T. L. & Keller, P. J. Mytilus byssal threads as an environmental marker for metals. *Aquatic Toxicology* **1**, 291-300, (1981).

32 Harrington, M. J. *et al.* Pseudoelastic behaviour of a natural material is achieved via reversible changes in protein backbone conformation. *J. R. Soc. Interface* **9**, 2911-2922, (2012).

33 Takeuchi, H. Raman structural markers of tryptophan and histidine side chains in proteins. *Biopolymers* **72**, 305-317, (2003).

34 Zhou, L. *et al.* Interaction between histidine and zn(ii) metal ions over a wide ph as revealed by solid-state nmr spectroscopy and dft calculations. *J. Phys. Chem. B* **117**, 8954-8965, (2013).

35 Hashimoto, S., Ono, K. & Takeuchi, H. Uv resonance raman scattering from metal-coordinating histidine residues in cu,zn-superoxide dismutase. *J. Raman Spectrosc.* **29**, 969-975, (1998).

36 Wang, D., Zhao, X., Vargek, M. & Spiro, T. G. Metal-bound histidine modes in uv resonance raman spectra of cu, zn superoxide dismutase. *J. Am. Chem. Soc.* **122**, 2193-2199, (2000).

37 Miura, T., Suzuki, K., Kohata, N. & Takeuchi, H. Metal binding modes of alzheimer's amyloid β-peptide in insoluble aggregates and soluble complexes. *Biochemistry* **39**, 7024-7031, (2000).

38 Jehle, F., Fratzl, P. & Harrington, M. J. Metal-tunable self-assembly of hierarchical structure in mussel-inspired peptide films. *ACS Nano* **12**, 2160-2168, (2018).

39 Trapaidze, A., D'Antuono, M., Fratzl, P. & Harrington, M. J. Exploring mussel byssus fabrication with peptide-polymer hybrids: Role of ph and metal coordination in self-assembly and mechanics of histidine-rich domains. *Eur. Polym. J.* **109**, 229-236, (2018).

40 Tunn, I., Harrington, M. J. & Blank, K. G. Bioinspired histidine–zn2+ coordination for tuning the mechanical properties of self-healing coiled coil cross-linked hydrogels. *Biomimetics* **4**, 25, (2019).

41 Hafsa, N. E., Arndt, D. & Wishart, D. S. Csi 3.0: A web server for identifying secondary and super-secondary structure in proteins using nmr chemical shifts. *Nucleic Acids Res.* **43**, W370-W377, (2015).

42 Shen, Y. & Bax, A. Protein backbone and sidechain torsion angles predicted from nmr chemical shifts using artificial neural networks. *J. Biomol. NMR* **56**, 227-241, (2013).

43 Shen, Y. & Bax, A. Protein structural information derived from nmr chemical shift with the neural network program talos-n. *Methods Mol. Biol.* **1260**, 17-32, (2015).

44 Raum, H. N., Modig, K., Akke, M. & Weininger, U. Proton transfer kinetics in histidine side chains determined by ph-dependent multi-nuclear nmr relaxation. *J. Am. Chem. Soc.* **146**, 22284-22294, (2024).

45 Tan, Y. J., Oliveberg, M., Davis, B. & Fersht, A. R. Perturbed pka-values in the denatured states of proteins. *J. Mol. Biol.* **254**, 980-992, (1995).

46 Zarycz, M. N. C. & Fonseca Guerra, C. Nmr 1h-shielding constants of hydrogen-bond donor reflect manifestation of the pauli principle. *J. Phys. Chem. Lett.* **9**, 3720-3724, (2018).

47 Lim, J. *et al.* Liquid–liquid phase separation of short histidine- and tyrosine-rich peptides: Sequence specificity and molecular topology. *J. Phys. Chem. B* **125**, 6776-6790, (2021).

48 Gabryelczyk, B. *et al.* Hydrogen bond guidance and aromatic stacking drive liquid-liquid phase separation of intrinsically disordered histidine-rich peptides. *Nat. Commun.* **10**, 5465, (2019).

49 Shin, Y. & Brangwynne Clifford, P. Liquid phase condensation in cell physiology and disease. *Science* **357**, eaaf4382, (2017).

50 Šneiderienė, G. *et al.* Lipid-induced condensate formation from the alzheimer’s aβ peptide triggers amyloid aggregation. *Proc. Natl. Acad. Sci. U.S.A.* **122**, e2401307122, (2025).

51 Dutour-Provenzano, G. & Etienne-Manneville, S. Intermediate filaments. *Curr. Biol.* **31**, R522-R529, (2021).

52 Sapra, K. T. *et al.* Nonlinear mechanics of lamin filaments and the meshwork topology build an emergent nuclear lamina. *Nat. Commun.* **11**, 6205, (2020).

53 Miserez, A. & Guerette, P. A. Phase transition-induced elasticity of α-helical bioelastomeric fibres and networks. *Chem. Soc. Rev.* **42**, 1973-1995, (2013).

54 Schmidt, S. *et al.* Metal-mediated molecular self-healing in histidine-rich mussel peptides. *Biomacromolecules* **15**, 1644-1652, (2014).

55 Cao, Y., Yoo, T. & Li, H. Single molecule force spectroscopy reveals engineered metal chelation is a general approach to enhance mechanical stability of proteins. *Proc. Natl. Acad. Sci. U.S.A.* **105**, 11152-11157, (2008).

56 Tunn, I., de Léon, A. S., Blank, K. G. & Harrington, M. J. Tuning coiled coil stability with histidine-metal coordination. *Nanoscale* **10**, 22725-22729, (2018).

57 Carrington, E., Waite, J. H., Sarà, G. & Sebens, K. P. Mussels as a model system for integrative ecomechanics. *Ann. Rev. Mar. Sci.* **7**, 443-469, (2015).

58 Rief, M., Gautel, M., Oesterhelt, F., Fernandez, J. M. & Gaub, H. E. Reversible unfolding of individual titin immunoglobulin domains by afm. *Science* **276**, 1109-1112, (1997).

59 Chen, Q., Chen, H., Zhu, L. & Zheng, J. Fundamentals of double network hydrogels. *J. Mater. Chem. B* **3**, 3654-3676, (2015).

60 Gong, J. P. Why are double network hydrogels so tough? *Soft Matter* **6**, 2583-2590, (2010).

61 Lee, H., Scherer, N. F. & Messersmith, P. B. Single-molecule mechanics of mussel adhesion. *Proc. Natl. Acad. Sci. U.S.A.* **103**, 12999-13003, (2006).

62 Priemel, T. *et al.* Compartmentalized processing of catechols during mussel byssus fabrication determines the destiny of dopa. *Proc. Natl. Acad. Sci. U.S.A.* **117**, 7613, (2020).

63 Lengerer, B. *et al.* Organ specific gene expression in the regenerating tail of macrostomum lignano. *Dev. Biol.* **433**, 448-460, (2018).

64 Duthoo, E. *et al.* Diversity and evolution of tyrosinase enzymes involved in the adhesive systems of mussels and tubeworms. *iScience* **27**, 111443, (2024).

65 Abramson, J. *et al.* Accurate structure prediction of biomolecular interactions with alphafold 3. *Nature* **630**, 493-500, (2024).

66 Chai Discovery, t. *et al.* Chai-1: Decoding the molecular interactions of life. *bioRxiv*, 2024.2010.2010.615955, (2024).

67 Hall, T. A. Bioedit: A user-friendly biological sequence alignment editor and analysis program for windows 95/98/nt. *Nucleic Acids Symposium Series* **41**, 95-98, (1999).

68 Alzohairy, A. Bioedit: An important software for molecular biology. *GERF Bull. Biosci.* **2**, 60-61, (2011).

69 Voehler, M. W., Collier, G., Young, J. K., Stone, M. P. & Germann, M. W. Performance of cryogenic probes as a function of ionic strength and sample tube geometry. *J. Magn. Reson.* **183**, 102-109, (2006).

70 Wishart, D. S. *et al.* 1h, 13c and 15n chemical shift referencing in biomolecular nmr. *J. Biomol. NMR* **6**, 135-140, (1995).

71 Markley, J. L. *et al.* Recommendations for the presentation of nmr structures of proteins and nucleic acids. Iupac-iubmb-iupab inter-union task group on the standardization of data bases of protein and nucleic acid structures determined by nmr spectroscopy. *J. Biomol. NMR* **12**, 1-23, (1998).

72 Ammann, C., Meier, P. & Merbach, A. A simple multinuclear nmr thermometer. *J. Magn. Reson.* **46**, 319-321, (1982).

73 Oregioni, A., Stieglitz, B., Kelly, G., Rittinger, K. & Frenkiel, T. Determination of the pka of the n-terminal amino group of ubiquitin by nmr. *Sci. Rep.* **7**, 43748, (2017).

74 Wallace, M., Adams, D. J. & Iggo, J. A. Titrations without the additions: The efficient determination of pka values using nmr imaging techniques. *Anal. Chem.* **90**, 4160-4166, (2018).

**Editor's Summary**

Mussels are masters of sticking on wet surfaces. Here, authors discover a histidine-rich coiled coil protein in mussel glue that challenges the prevailing understanding of how mussel stick tight, with the findings relevant to the design of improved glues.

**Peer review information:** *Nature Communications* thanks Chuang Liu and the other, anonymous, reviewer(s) for their contribution to the peer review of this work. A peer review file is available.